



# 1 Dynamical precursors to summer temperature extremes on 2 the Antarctic Peninsula

3

4 William J. Dow<sup>1</sup>, Amanda C. Maycock<sup>1</sup>, Andrew N. Ross<sup>1</sup>, Ryan S. Williams<sup>2</sup>, Thomas J.  
5 Bracegirdle<sup>2</sup>

6

7 1 - Institute for Climate and Atmospheric Sciences, School of Earth, Environment and Sustainability,  
8 University of Leeds, Leeds, UK

9 2 - British Antarctic Survey, Cambridge, UK

10

11 *Correspondence to:* William J. Dow ([earwd@leeds.ac.uk](mailto:earwd@leeds.ac.uk))

12

13 **Abstract:** Extreme warm summer near-surface temperatures over the Antarctic Peninsula (AP) can lead  
14 to surface melting and the disintegration of ice shelves. While individual case studies have linked such  
15 events to anomalous large-scale circulation, a systematic assessment of the dynamical pathways leading  
16 to AP-wide extreme austral summer warm events remains limited. This study uses ERA5 reanalysis data  
17 to investigate the large-scale dynamical precursors associated with extreme warm days over the Antarctic  
18 Peninsula. We apply k-means clustering to mean sea level pressure anomalies during high temperature  
19 extremes and identify five distinct circulation patterns with different dominant zonal wavenumbers. We  
20 investigate the spatio-temporal evolution and persistence of near-surface wind, temperature and pressure  
21 for each cluster. Four clusters are associated with rapidly amplifying planetary-scale wave patterns, while  
22 a fifth resembles a negative Southern Annular Mode-like state with enhanced persistence prior to event  
23 onset. Despite these differing pathways, all regimes promote anomalous northerly flow toward the AP,  
24 driving strong meridional temperature advection and regional warming. We demonstrate that extreme  
25 Antarctic Peninsula warm events arise from distinct circulation pathways, reflecting diverse dynamical  
26 states likely influenced by hemispheric-scale teleconnections and planetary wave interactions.

27

## 28 1 Introduction

29 The Antarctic Peninsula (AP) has undergone marked multi-decadal variability in surface air temperature  
30 since the mid-20th century. Warming trends calculated over periods longer than approximately 30 years  
31 appear robust, particularly during austral summer and autumn (González and Fortuny, 2018), with late  
32 20th century increases exceeding the global mean in several observational records (Marshall et al., 2006;  
33 Oliva et al., 2017; Wang et al., 2022a). Concurrently, the late 1990s marked the onset of a period of  
34 relative cooling consistent with internal variability (Carrasco et al., 2019; Turner et al., 2016). However,  
35 more recent analyses suggest that this early 21st century cooling may be weakening, with temperature



36 evolution closely tied to changes in large-scale circulation modes and regional pressure systems  
37 (Carrasco et al., 2019; Bozkurt et al., 2020).

38 During austral summer (December-February), episodes of extreme warm surface air temperatures over  
39 the AP — frequently exceeding 0 °C — are projected to become increasingly common under future  
40 scenarios that include continued increases in greenhouse gases (e.g. Siegert et al. 2019). Similarly,  
41 pronounced increases in high extremes (p90; 90th percentile compared to mean background climate) in  
42 precipitation and westerly wind anomalies are projected to occur on the AP over the 21st century  
43 compared to increases in background climatology (Bracegirdle et al., 2024). Such extreme weather  
44 events can drive surface melt (Gorodetskaya et al. 2023), firn air depletion (Dunmire et al. 2024), and, in  
45 some cases, contribute to the destabilisation and collapse of ice shelves (Scambos et al., 2009; Wille et  
46 al., 2022). Improving our understanding of the atmospheric drivers of extreme warm temperatures is  
47 therefore critical for assessing Antarctica’s vulnerability to climate change and its broader implications for  
48 the Earth system.

49 Extreme warm events over the AP are typically associated with strong poleward meridional wind  
50 anomalies near the AP at synoptic timescales, which are often associated with atmospheric blocking,  
51 atmospheric rivers and enhanced moisture transport towards Antarctica (Banwell et al., 2021; Bozkurt et  
52 al., 2024; Gorodetskaya et al., 2023; Wille et al., 2022; Zou et al., 2023; Wang et al., 2022a; Wang et al.,  
53 2022b). The synoptic scale circulation anomalies can be linked with remote forcing, and their effects on  
54 temperature may be modulated by local scale processes, including föhn warming on the eastern  
55 Peninsula (Bevan et al., 2020; Bae et al., 2022; Guarino et al., 2026; Kirchgassner et al., 2021; Xu et al.,  
56 2021; Zou et al., 2023).

57 Anomalous tropical convection associated with the Madden–Julian Oscillation (MJO) and the El Niño–  
58 Southern Oscillation (ENSO) can initiate poleward propagating Rossby wave trains that favour blocking  
59 highs over the South Pacific and Drake Passage (Renwick and Revell, 1999; Tseng et al., 2019; Clem et  
60 al., 2022; Barrett et al., 2025). In addition, a Rossby wave train from the tropical Atlantic has been shown  
61 to modulate the intensity of the Amundsen–Bellingshausen Seas Low (ABSL) on decadal timescales,  
62 thereby priming the regional circulation to influence conditions across the AP (Li et al., 2014; Li et al.,  
63 2015). Furthermore, anomalous sea surface temperatures across the South Pacific Convergence Zone  
64 (SPCZ) have been linked to anticyclonic blocking over coastal West Antarctica through enhanced Rossby  
65 wave propagation (Deb et al., 2025). Together, these tropical-extratropical teleconnections can promote  
66 poleward transport of heat and moisture toward the Peninsula (e.g., Rondanelli et al., 2019; Clem et al.,  
67 2022).

68 Atmospheric circulation near the AP is also modified by the Southern Annular Mode (SAM) (e.g. Fogt et  
69 al., 2012; Clem and Fogt, 2013; Clem et al., 2016; Montano Bello and Villegas Bolanos, 2025). Post  
70 1979, the SAM has become less zonally symmetric, with an increase in zonal wave-3 structure and an



71 eastward shift in phase, resulting in more northerly flow over the AP during positive SAM conditions,  
72 consistent with an eastward displacement of the Amundsen–Bellingshausen Sea Low (Marshall et al.,  
73 2022). The SAM has also exhibited a positive trend in austral summer and autumn since the late 20th  
74 century, with the summer trend driven primarily by stratospheric ozone depletion (e.g. Thompson and  
75 Solomon, 2002; Marshall et al., 2003; Fogt and Marshall, 2020), alongside a deepening of the ABSL  
76 (England et al., 2016). The shift toward more positive summer SAM conditions has contributed to long-  
77 term warming over the AP through the intensification of high-latitude cyclones, strengthening of  
78 meridional flow onto the AP via amplification of the ABSL, and enhancement of lee-side föhn winds along  
79 the eastern AP (Marshall, 2007; Orr et al., 2008; Fogt et al., 2011, 2012; Turner et al., 2013; Hosking et  
80 al., 2013). Importantly, SAM variability has been linked to changes in the frequency of Peninsula-centred  
81 pressure dipole patterns and ABSL-dominated regimes (Hosking et al., 2013; Raphael et al., 2016),  
82 including an increased occurrence of an AP-centred dipole during summer between 1979 and 2016  
83 (González et al., 2018)

84 While the typical circulation features necessary to drive anomalous high temperatures over the AP have  
85 been described in the literature (e.g. Balay and Renom, 2026; Clem et al., 2022; Gorodetskaya et al.,  
86 2023; Wang et al., 2022a; Wille et al., 2022), there has been relatively little investigation into the diversity  
87 in circulation features amongst extremes. In particular: are all dynamically-driven AP extremes made  
88 equal? Gonzalez et al. (2018) performed daily clustering of circulation patterns around the AP during the  
89 entire year, and therefore did not isolate circulation features associated with extreme high temperatures.  
90 Nielsen et al. (2025) applied clustering to surface air temperature trends over the entire Antarctic  
91 continent which identified a single cluster representing the AP with its associated extremes, and therefore  
92 did not consider the diversity of circulation features amongst AP temperature extremes. As a result, a  
93 systematic characterisation of the circulation pathways producing summer high temperatures over the AP  
94 is lacking.

95 This study uses ERA5 reanalysis data to examine the synoptic and large-scale circulation patterns linked  
96 to extreme austral summer temperature events across the AP. We define extremes over the AP and  
97 apply k-means clustering (cf. Nielsen et al., 2025) to mean sea level pressure (MSLP) anomalies at the  
98 onset of the extreme temperatures to identify their characteristic clusters which are then studied. The  
99 remainder of the paper is structured as follows: Section 2 outlines the methods, Section 3 presents the  
100 results, and Section 4 discusses the implications for understanding and anticipating future extreme events  
101 in a warming climate.

## 102 **2 Data and Methods**

103

### 104 **2.1 Data**

105



106 Daily mean near-surface air temperature, 10 metre wind fields, sea level pressure and 500 hPa  
107 geopotential height data were obtained from ERA5 for the period 1979-2024 on a regular  $0.25^\circ \times 0.25^\circ$   
108 grid (Hersbach et al., 2020). Hourly zonal and meridional winds and temperature fields at 300 hPa were  
109 utilised in the meridional temperature advection analysis. ERA5 exhibits regionally varying near-surface  
110 biases at coastal stations and a general warm bias (DJF mean = +0.96 K) (Zhu et al. 2021) over the AP;  
111 however, it demonstrates generally high agreement in temporal variability with Antarctic station  
112 observations (DJF seasonal mean correlation coefficient = 0.82) (Zhu et al., 2021) and is considered to  
113 effectively capture the spatial structure and temporal variability of near surface temperature and  
114 circulation climate across the AP (Tetzner et al., 2019; Hillebrand et al., 2020; Zhu et al., 2021). This  
115 makes ERA5 well suited for analysing synoptic scale circulation associated with austral summer  
116 temperature extremes across the AP.

117

## 118 **2.2 Methods**

119

### 120 **2.2.1 Definition of temperature extremes**

121

122 Extreme high temperature days are identified based on 2-m temperature anomalies calculated relative to  
123 a 21-day running mean climatology. Alternative climatological window lengths (7, 10, 14, 30 days) were  
124 tested (Supplementary Fig. S1), with 21 days chosen to best capture the seasonal cycle without  
125 oversmoothing. The AP temperature anomalies are then calculated as the area-weighted average over  
126 the whole region [80°W-50°W; 60°S-75°S]. Extreme summer temperature anomalies are defined as days  
127 when the temperature anomaly exceeds the DJF 95th percentile of departures from the 21-day running  
128 mean. This approach aims to capture coherent high temperature events which have the potential to  
129 impinge on ice shelf surface melting, and are most likely driven by large-scale regional circulation  
130 anomalies (e.g. Wille et al., 2022). The seasonal DJF temperature trend over 1979-2024 is not significant  
131 across the AP region in ERA5 (Zhu et al., 2021), and we find no systematic trend in the frequency of  
132 extreme high temperature days during the analysis period (Supplementary Fig S2).

133 Extreme high temperature days are grouped into events allowing up to 2 consecutive non-extreme days  
134 within a sequence (cf. Baldwin et al., 2019; Ruosteenoja & Jylhä, 2023). Sequences separated by >2  
135 days were treated as independent events. This definition captures 87 events (mean duration 2.4 days),  
136 with most lasting one day ( $n = 35$ , 40%) and 82% lasting three days or fewer.

137

### 138 **2.2.2 K-means clustering**

139

140 K-means clustering has been applied to understand Antarctic climate in previous work (Coggins et al.,  
141 2014; Nielsen et al., 2025; Gonzalez et al., 2018). Here, we apply k-means clustering using Lloyd's



142 algorithm, to the daily MSLP anomaly fields over the region [50°S - 90°S, 180°W - 0°W] for days -3 to +1  
143 relative to the event onset (day 0). The -3 to +1 day window is chosen to capture the immediate synoptic  
144 evolution preceding and during extreme high temperature events, while limiting the inclusion of unrelated  
145 background variability. Each day within this window is treated as an independent sample in the clustering  
146 procedure. That is, daily MSLP anomaly fields from all events spanning days -3 to +1 are input to the  
147 clustering. This allows the temporal evolution of circulation patterns leading up to event onset to be  
148 assessed through the event duration.

149

150 Lloyd's algorithm is iterative and centroid-based, partitioning the dataset  $X$  containing  $n$  observations into  
151  $K$  distinct groups  $C_K$ , such that each day is assigned to the cluster with the nearest centroid  $U_K$ . The goal  
152 is to reduce the total within-cluster variance by minimizing the sum of the squared distance between each  
153 data point and the center of its assigned cluster. Mathematically, this is expressed as:

154

$$155 \quad \sum_{k=1}^K \sum_{x_n \in C_k} |x_n - \mu_k|^2 \quad (1)$$

156

157

158 Starting from an initial set of centroids, the algorithm first assigns each data point to the cluster whose  
159 centroid is nearest in terms of distance:

160

$$161 \quad C_K = \{x_n : |x_n - \mu_k| \leq \text{all } |x_n - \mu_l|\} \quad (2)$$

162

163

164 Then, for the given clusters, the centroids are repositioned to the mean of all points belonging to each  
165 cluster:

166

$$167 \quad u_k = \frac{1}{C_k} \sum_{x_n \in C_k} x_n \quad (3)$$

168

169 This iterative process continues until they converge, minimising the sum of squares in the clustering  
170 arrangement. We determined the optimal number of clusters ( $k = 5$ ) using the silhouette coefficient  
171 (Supplementary Figure S3) (Rousseeuw, 1987). We further tested ( $k = 4$ ) and ( $k = 6$ ) observing that  
172 two of the five clusters identified at ( $k = 5$ ) merged into a single cluster at ( $k = 4$ ) while one cluster from  
173 ( $k = 5$ ) split into two distinct clusters at ( $k = 6$ ) (Supplementary Figs. S4 and S5).

174

175

176 **2.2.3 Horizontal thermal advection**



177

178 Horizontal thermal advection was calculated using ERA5 reanalysis data at hourly resolution (see Section  
179 2.1) following the formula:

180

$$181 \quad -v \cdot \nabla_p T = - \left( u \left( \frac{\delta T}{\delta x} \right)_p + v \left( \frac{\delta T}{\delta y} \right)_p \right) \quad (4)$$

182

183 Where  $\nabla_p$  denotes the horizontal gradient on a constant pressure surface,  $u$  and  $v$  represent the zonal  
184 and meridional components of wind and  $T$  represents air temperature.

185

186 Temperature gradients are calculated using centred finite differences on the native grid, with grid spacing  
187 in units derived from spherical geometry assuming an Earth radius of 6371km. The results were  
188 converted to units of K day<sup>-1</sup>. To minimise the influence of orographic effects, the analysis was performed  
189 on a constant pressure level of 300 hPa.

190

### 191 **3 Results**

192

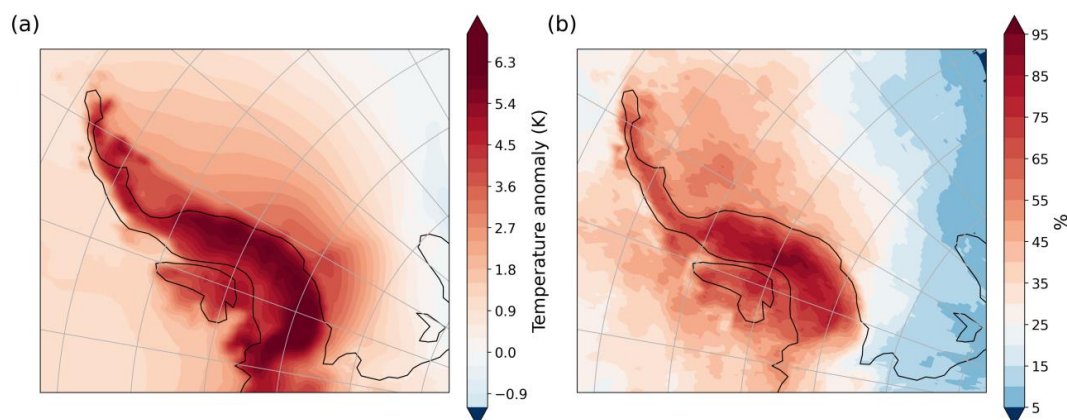
#### 193 **3.1 Spatial patterns of extreme high temperature events**

194

195 The composite 2-m temperature anomalies for high temperature extremes show spatially coherent  
196 positive temperature anomalies across the AP (Figure 1a), with typical magnitudes exceeding 4 K. Figure  
197 1b shows the extreme events identified based on the 95th percentile of AP average 2-m temperature  
198 coincide with local temperature anomalies above the 95th percentile on average at least 50% of the time  
199 at most locations. Coherence is strongest across the central and southern AP, with somewhat weaker  
200 correspondence toward the northern tip. The presence, on average, of high temperature anomalies  
201 across the entire AP in the set of extreme events confirms they are typically large-scale events that are  
202 likely to have a primary origin from synoptic scale atmospheric circulation drivers.

203

204



205

206

207 **Figure 1: (a) Composite daily mean 2m temperature anomalies over the Antarctic Peninsula on**

208 **summer days where the temperature exceeds the 95th percentile. (b) Percentage of extreme**

209 **events (see Methods) from (a) during which the local 2m temperature exceeds the local 95th**

210 **percentile threshold at least once.**

211

### 212 **3.2 Circulation clusters for high temperature events**

213

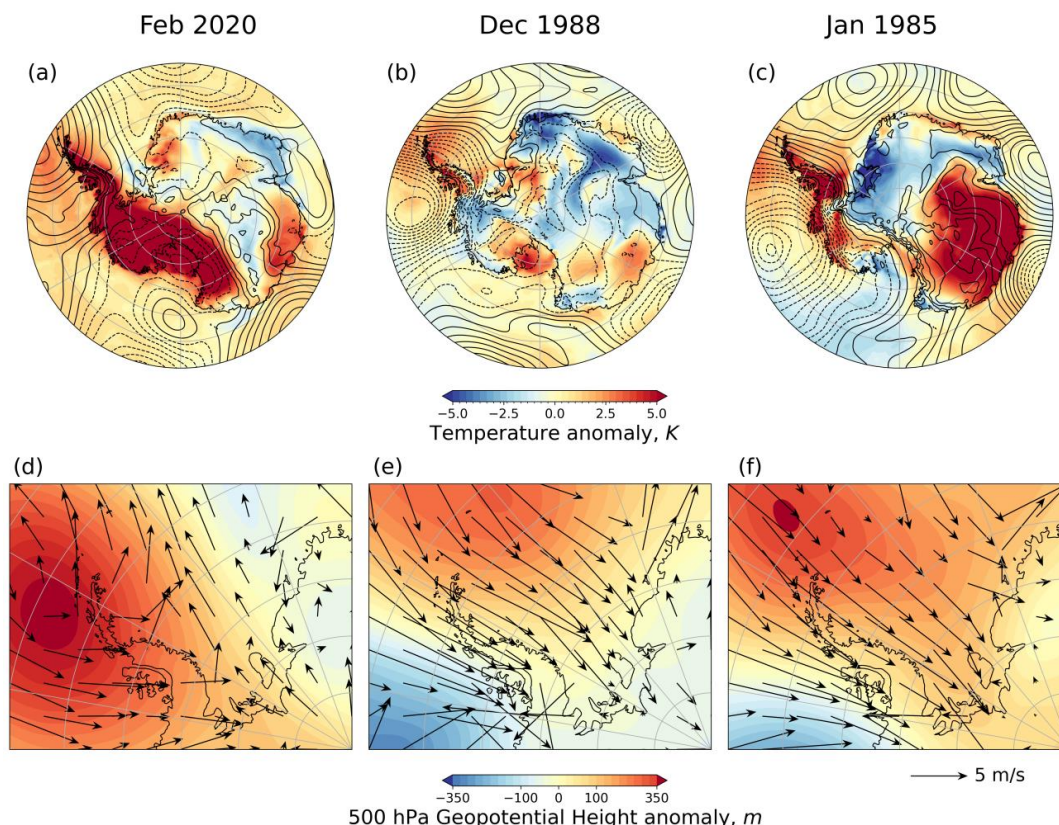
214 To motivate the applicability of k-means clustering to distinguish circulation patterns associated with  
 215 extreme high temperature events over the AP, we first review three well-documented case studies. Figure  
 216 2a–c shows daily 2-m temperature anomalies for: 6–11th February 2020 - the record breaking heatwave  
 217 over AP triggered by deep convection in the central tropical Pacific (González-Herrero et al., 2022; Clem  
 218 et al., 2022); 31st December 1988; and 25th January 1985 - corresponding to extreme warm days  
 219 recorded at the Faraday/Vernadsky station on the west of the Peninsula (Turner et. al., 2020). The  
 220 temperature anomalies during the three events exhibit pronounced spatial heterogeneity and duration.  
 221 Coincident with the February 2020 event (Fig. 2a), positive anomalies exceeding +5 K were observed  
 222 across Southwest and West Antarctica (WA), whereas over Dronning Maud Land (DML) and East  
 223 Antarctica (EA) temperatures remained near climatology. The AP warming coincided with an anomalous  
 224 ridge positioned to the west of the AP and associated westerly wind anomalies of approximately  $3 \text{ m s}^{-1}$   
 225 (Fig. 2d). In contrast, the extreme warm event in December 1988 (Fig. 2b) was more confined to the AP,  
 226 with coincident negative temperature anomalies across central and EA and weaker warm anomalies over  
 227 Queen Mary Land and the Ross Ice Shelf. This event is characterised by a dipole MSLP anomaly  
 228 straddling the AP, with a ridge extending along its axis and anomalous northwesterly flow exceeding  
 229  $5 \text{ m s}^{-1}$ . The January 1985 event (Fig. 2c) coincided with widespread positive temperature anomalies that  
 230 extended across EA. The corresponding MSLP and near-surface wind anomalies (Fig. 2f) resemble those  
 231 of the December 1988 event, although the high-pressure centre is displaced closer to the AP and shifted



232 westward. The contrasting spatial footprints and circulation anomalies associated with these events serve  
 233 to highlight the diversity of regional circulation patterns driving extreme high temperatures on the AP and  
 234 their related anomalies across the continent.

235

236



237

238 **Figure 2: Three extreme warm summer events recorded across AP. (a, d) 6th-11th February 2020,**  
 239 **(b, e) 31st December 1988, (c, f) 25th January 1985. (a-c) Shading: daily near-surface temperature**  
 240 **anomalies; contours: MSLP anomalies (interval 2 hPa, solid = positive, dashed = negative). (d-f)**  
 241 **Shading: 500 hPa geopotential height anomalies; vectors: near-surface winds [domain 280°E -**  
 242 **320°E, 60°S - 90°S].**

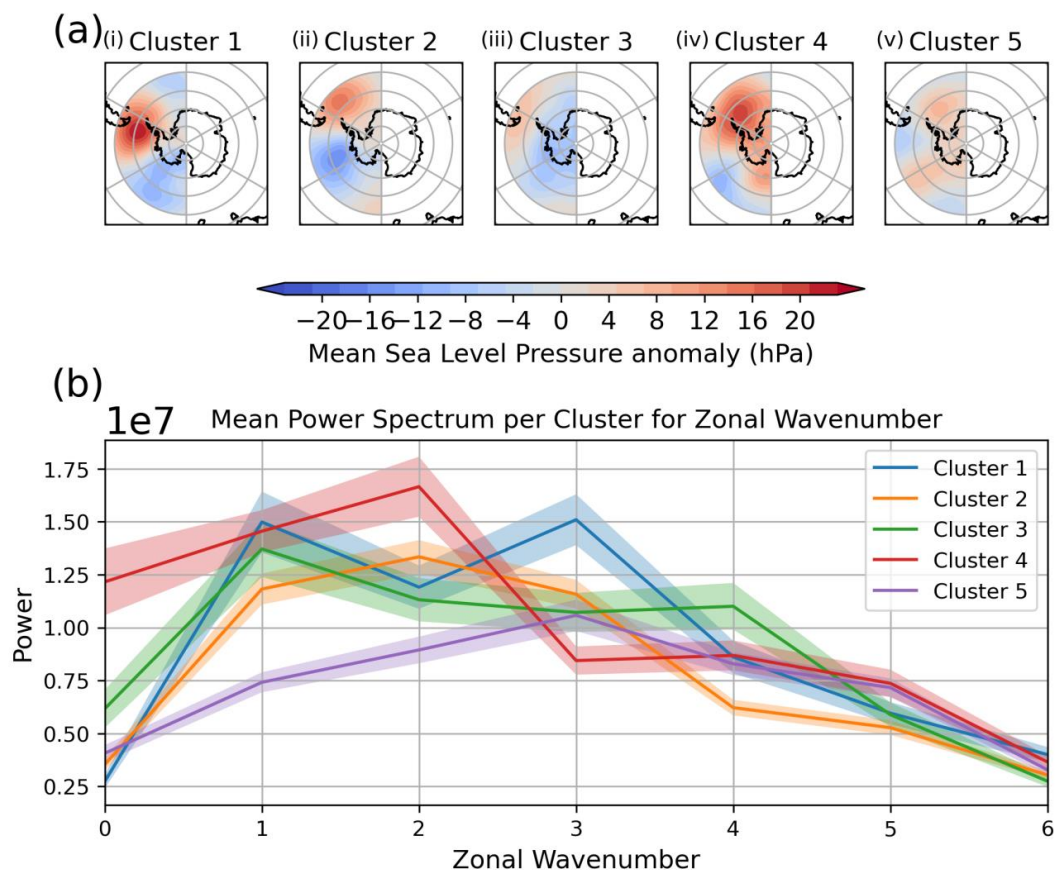
243

244 The MSLP anomalies associated with the five k-means cluster centroids are presented in Figure 3a.  
 245 Cluster 1 is characterised by a high pressure anomaly centred over the Drake Passage and a low  
 246 pressure anomaly centred between the Amundsen Sea and Ross Sea, with peaks in the mean power  
 247 spectrum at zonal wavenumbers 1 and 3. (Fig. 3ai, Fig. 3b). Cluster 2 exhibits a dipole structure  
 248 straddling the AP, consistent with a zonal wavenumber-2 pattern (Fig. 3aii). Cluster 3 features a broad



249 low pressure anomaly centred over the Amundsen Sea with negative anomalies extending over  
250 continental WA, with a peak in the mean power spectrum at zonal wavenumber 1 (Fig. 3aiii, Fig. 3b).  
251 Cluster 4 shows a peak in the mean power spectrum at zonal wavenumber 2 and is associated with high  
252 pressure across WA and the eastern Bellingshausen Sea and a pronounced anticyclone centred  
253 northeast of the AP (Fig. 3aiv, Fig. 3b). Cluster 5 displays a zonal wavenumber 3 pattern including a  
254 dipole flanking the AP (Fig. 3av).  
255  
256

### K-Means Cluster Centroids and Spectral Power



257  
258 **Figure 3: (a) Centroids (in hPa) for the 5 clusters shown across the hemisphere over which they**  
259 **were defined [50°S - 90°S, 180°E - 360°E]. (b) Composite average zonal wavenumber power**  
260 **spectrum for each cluster. Shading represents  $\pm 1$  standard error of the mean.**

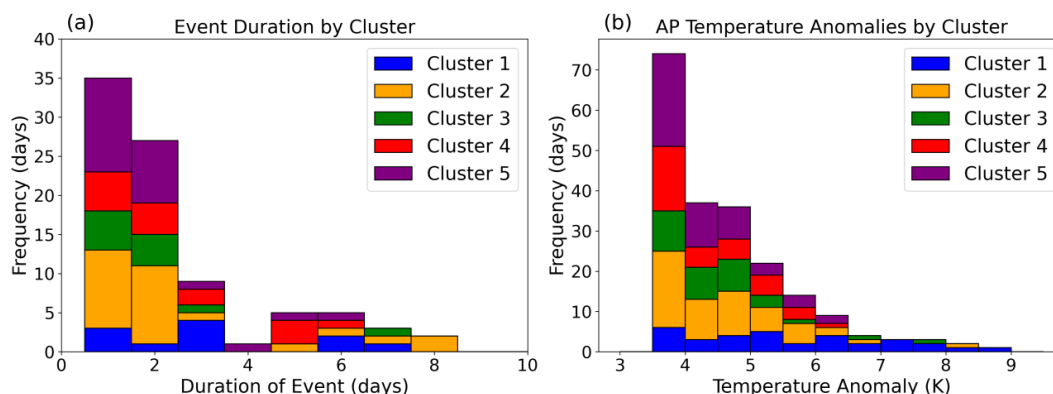
261  
262



263 **3.3 Temporal behaviour of high temperature events by cluster**

264

265



266

267

268

269

270

**Figure 4: (a) Histogram showing the duration of each extreme event separated by each k-means cluster. (b) Histogram showing the area-weighted mean 2-m temperature anomaly over the Antarctic Peninsula across all the days of the extreme high temperature events.**

271

272

273

274

275

276

277

278

279

Figure 4 summarises the differences between clusters in terms of event duration and the associated AP temperature anomalies, with the accompanying statistics presented in Table 1. Clear distinctions emerge in both the persistence and intensity of extreme high temperature events between the clusters. Cluster 1 comprises the longest and most intense events with durations ranging from 1 to 7 days and the largest mean AP temperature anomaly. In contrast, Clusters 2–4 represent intermediate-duration events with weaker mean anomalies compared to those from Cluster 1. Cluster 5, which contains the largest number of events, is characterised by the shortest durations and the weakest mean anomalies.

	Number of events (Percentage of total)	Mean length (days)	Mean temperature anomaly (K)
Cluster 1	11 (13%)	3.3±1.2	5.5±0.6
Cluster 2	26 (30%)	2.6±0.8	4.6±0.2
Cluster 3	11 (13%)	2.1±1.0	4.5±0.4
Cluster 4	15 (17%)	2.7±0.8	4.4±0.2



Cluster 5	24 (28%)	1.9±0.6	4.3±0.2
-----------	----------	---------	---------

280

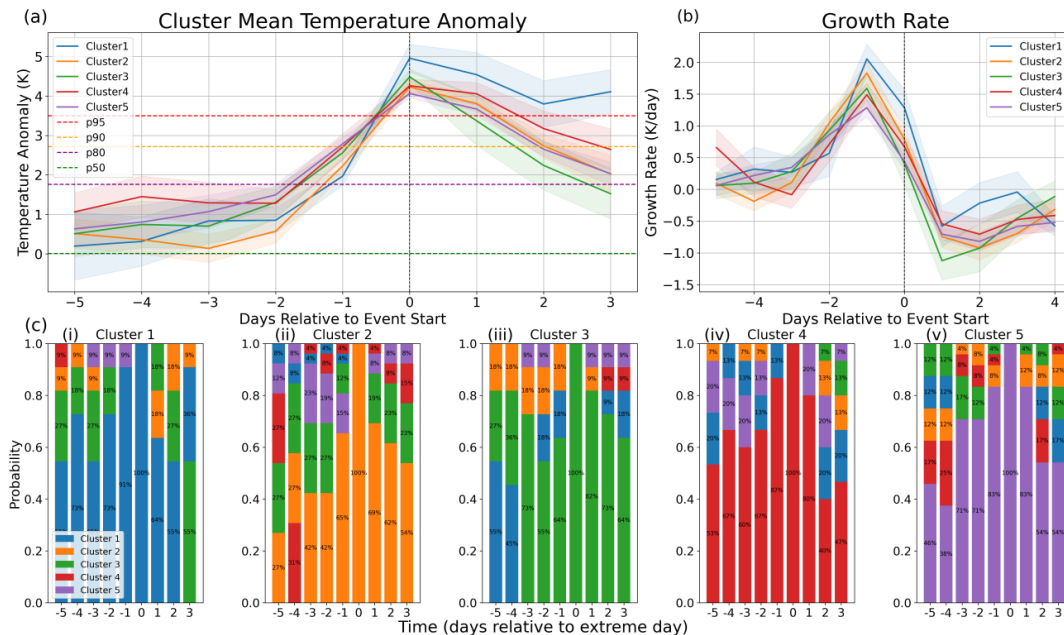
281 **Table 1: Summary of event statistics by cluster, including event duration and associated**  
 282 **temperature anomalies, highlighting differences in cluster characteristics. Uncertainty values**  
 283 **represent 95% confidence range.**

284

285 Figure 5a shows the temporal evolution of AP-mean temperature anomalies during extreme high  
 286 temperature events for each cluster, with the corresponding temperature growth rates, calculated using  
 287 centred finite differences, shown in Fig. 5b. Temperature anomalies remain below 2 K for all clusters until  
 288 two days prior to onset. At this point, Clusters 3–5 exhibit steadily increasing anomalies, reaching peaks  
 289 of approximately 4.0–4.5 K at day 0. By contrast, Cluster 1 shows weaker anomalies during days -2 to  
 290 -1, followed by a rapid intensification in the final day before onset, with growth rates approaching ~2 K  
 291 day<sup>-1</sup> and peak anomalies near 5 K. Cluster 2 also exhibits rapid pre-onset growth but attains a slightly  
 292 lower peak (~4.3 K), representing, on average, a fast-developing yet more moderate extreme event.

293

294



295

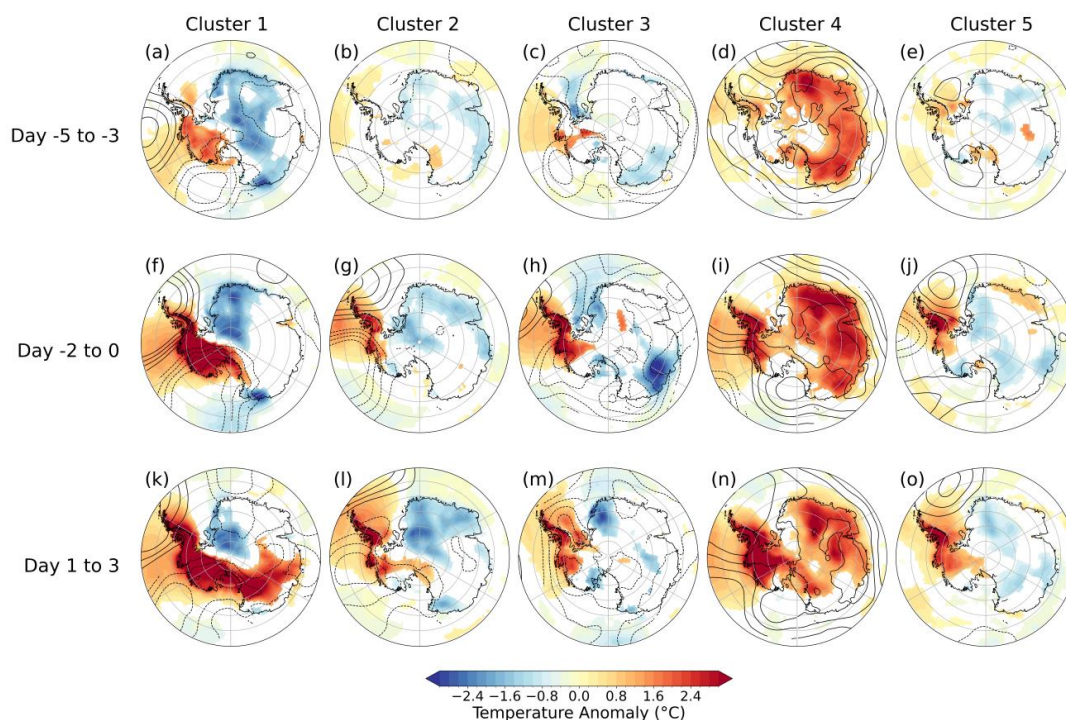
296 **Figure 5: (a) Mean temperature anomaly across the Antarctic Peninsula for the events in each**  
 297 **cluster between days -5 and +3. (b) As in (a) but for average temperature growth rate (dT/dt).**



298 **Shading represents  $\pm 1$  standard error of the mean. (c) Fraction of events in each cluster whose**  
299 **circulation patterns are assigned to all clusters as a function of lag. Percentages shown in the**  
300 **bars give the proportion of days classified to each cluster. Bars are ordered by decreasing**  
301 **fraction.**

302 Figure 5c shows the fraction of events assigned to each cluster at day 0 that are assigned to all clusters  
303 at different lead and lag times. By construction, 100% of events are assigned to their respective clusters  
304 at day 0. Only 55% of Cluster 1 events are assigned to the same cluster at day -5, indicating substantial  
305 variability in circulation in the lead-up to the extreme event. Cluster coherence on day -5 is lower for  
306 Clusters 2 (28%) and 3 (27%), but higher for Cluster 4 (53%). Cluster 3 exhibits higher coherence at day  
307 -3 (78%), although this fraction declines at days -2 and -1, suggesting that the circulation patterns  
308 associated with many events are located between centroids prior to onset. Similar temporal evolution is  
309 observed for Clusters 1, 4, and 5 in the days preceding onset, with Cluster 5 showing the highest  
310 persistence, as 70% of events retain their cluster assignment at day -3. Together, these results indicate  
311 that some clusters represent relatively stable, long-lived large-scale circulation anomalies (e.g., Cluster  
312 5), whereas others are characterised by rapidly evolving or transitional synoptic conditions leading up to  
313 extreme high temperature events.

314 To further explore this temporal evolution, Figure 6 shows composites of MSLP and 2-m temperature  
315 anomalies for the days preceding, during and following the onset of the extreme high temperature events  
316 for each cluster. The composite MSLP anomalies closely resemble the respective centroids, reinforcing  
317 the robustness of the k-means classification. The associated temperature anomaly patterns display  
318 substantial differences in spatio-temporal structure between the clusters.  
319  
320



321

322 **Figure 6: Time-averaged lagged composites of events in each cluster for (a-e) days -5 to -3; (f-j)**  
 323 **days -2 to 0 and (k-o) days 1 to 3. Day 0 = first day of the extreme event. Shading: near-surface**  
 324 **temperature anomalies; contours: MSLP anomalies (interval 2 hPa, solid = positive, dashed =**  
 325 **negative). Non-significant anomalies ( $p > 0.05$ ) are not plotted.**

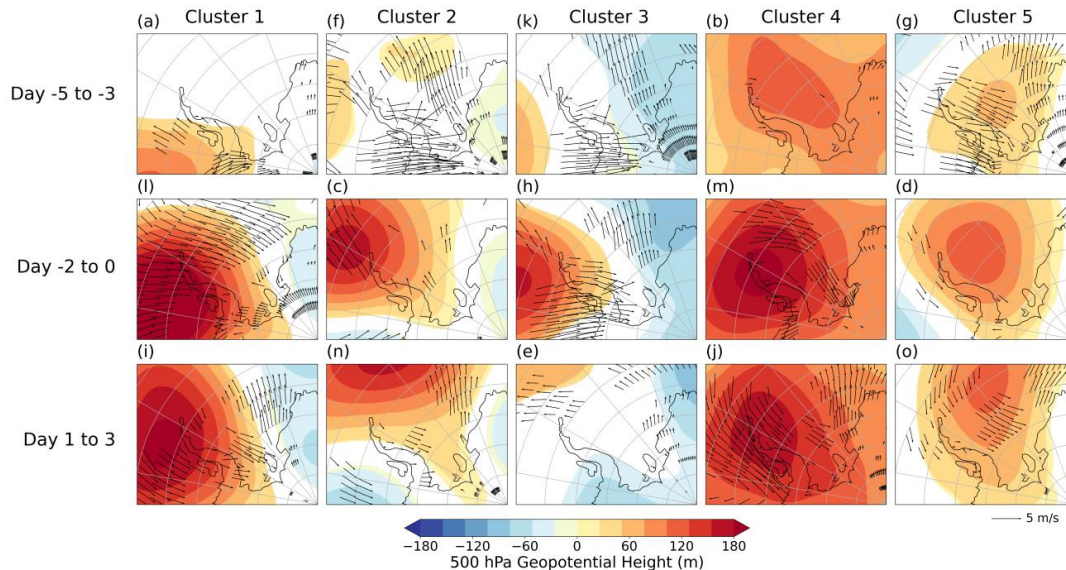
326 Fig. 6a-e shows composite anomalies over days -5 to -3 prior to the onset of extreme warm conditions  
 327 across AP. In Cluster 1, the warming over WA evident at event onset is already established, though warm  
 328 anomalies are absent from AP (Fig. 6a). During Cluster 2 events, anomalies remain close to  
 329 climatological values over days -5 to -3 prior to onset (Fig. 6b). For Cluster 3, there is warming evident in  
 330 the Bellingshausen Sea and cooling across the Weddell Sea evident in the lead-up period (Fig. 6c). In  
 331 Cluster 4, there is continental wide warm anomalies with the exception of parts of WA prior to the onset of  
 332 extreme high temperatures on the AP (Fig. 6d). Temperature anomalies associated with Cluster 5 are  
 333 broadly close to climatological values prior to the onset of extreme high temperatures on the AP (Fig. 6e).

334 During the event onset phase (days -2 to 0), Cluster 1 exhibits widespread warm anomalies across the  
 335 AP, extending into WA and across the Ross Ice Shelf, while cold anomalies are present over Dronning  
 336 Maud Land (Fig. 6f). Following the event onset (days 1-3), the warm temperature anomalies extend  
 337 further across to East Antarctica (Fig. 6k) while the cold anomalies near the Dronning Maud Land return  
 338 towards climatology. Cluster 2 is characterised by warming over the AP and the Bellingshausen Sea,  
 339 accompanied by cooling at the South Pole and across coastal East Antarctica including Dronning Maud



340 Land (Fig. 6g). The warm anomalies expand into the Ross Ice Shelf area in the period after event onset,  
 341 with areas of EA characterised by an intensification of their cold anomalies (Fig. 6l). In Cluster 3, the  
 342 warm anomalies are largely restricted to the AP and WA, while cooling is observed over Wilkes Land (Fig.  
 343 6h). After the event onset, warming is largely confined to the same region whilst the cold anomalies found  
 344 over Wilkes Land return towards climatology (Fig. 6m). Cluster 4 exhibits extensive warm anomalies  
 345 spanning most of the Antarctic continent (Fig. 5i), which persist in the days following event onset (Fig.  
 346 6n). Cluster 5 shows warming over the AP, Weddell Sea and Bellingshausen Sea and cooling over much  
 347 of EA (Fig. 6j). Following the event, the warm anomalies grow across WA whilst cold anomalies persist  
 348 over much of EA (Fig. 6o).

349 Figure 7 shows composite 500 hPa geopotential height anomalies and 10-m wind anomalies over the AP  
 350 for days -5 to -3, -2 to 0, and 1 to 3 relative to the onset of high AP temperature events. Across all  
 351 clusters, there are positive mid-tropospheric height anomalies over or near the AP, indicating the  
 352 presence of an anomalous ridge, although the amplitude and position of the ridge varies between  
 353 clusters.



354  
 355 **Figure 7: As in Figure 6, but for 500 hPa geopotential height anomalies (shading) and near-surface**  
 356 **wind speed anomalies (vectors) for the sector 280°E - 320°E, 60°S - 90°S. Non-significant**  
 357 **anomalies ( $p > 0.05$ ) are not plotted.**

358

359 During the preconditioning phase (days -5 to -3), an anomalous ridge is established close to the AP, with  
 360 the high pressure centre located to the west and migrating eastward toward the AP by the onset phase

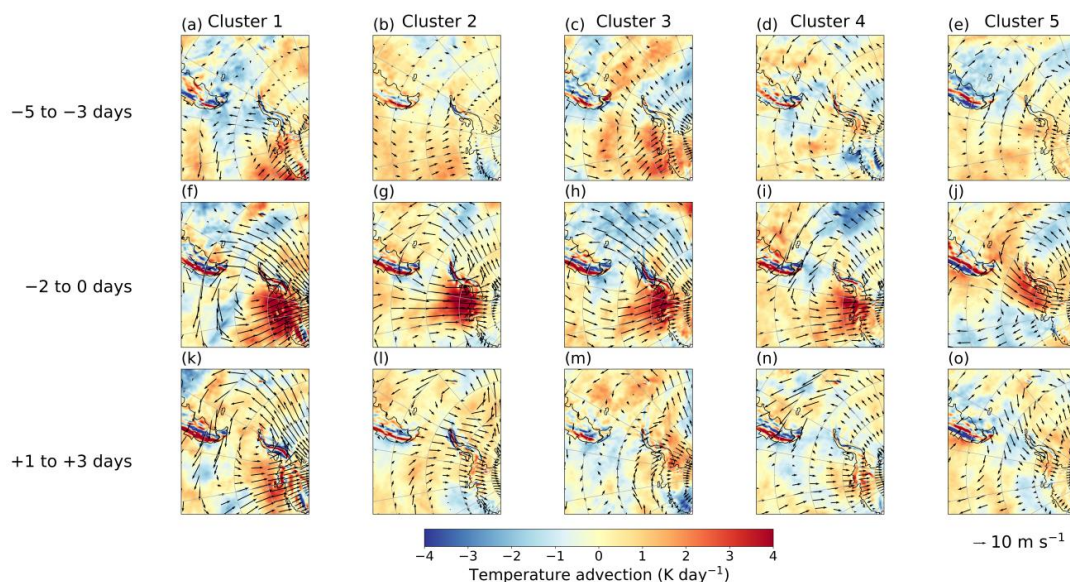


361 (days -2 to 0). An exception occurs in Clusters 4 and 5, where the high pressure centre is positioned to  
362 the east of the AP during preconditioning, placing the AP beneath the western flank of the ridge. 10-m  
363 wind anomalies exhibit substantial inter-cluster differences in both magnitude and direction. Cluster 1 is  
364 characterised by strong ( $\sim 5 \text{ m s}^{-1}$ ) and statistically significant northerly anomalies across the  
365 Bellingshausen Sea, Weddell Sea, and northern AP during event onset (Fig. 7l). These anomalies are  
366 approximately twice the magnitude of the climatological winds in this region, consistent with enhanced  
367 meridional warm-air advection. The wind anomalies weaken in the days following onset, while the ridge  
368 remains quasi-stationary. Clusters 3 and 4 also exhibit significant northerly anomalies of comparable  
369 magnitude, centred primarily over the Bellingshausen Sea (Cluster 3) and the Weddell Sea (Cluster 4)  
370 (Fig. 7h,m). Following onset, northerly anomalies in Cluster 4 intensify and expand to encompass much of  
371 the AP, whereas in Cluster 3 the ridge weakens and northerly anomalies largely dissipate. In contrast,  
372 Cluster 2 displays anomalous southerly near-surface winds offshore to the east of the AP (Weddell Sea)  
373 during event onset (Fig. 7c), and the associated ridge migrates northward away from the AP in the post-  
374 onset period. Cluster 5 exhibits relatively weak and spatially limited northerly anomalies at event onset  
375 (Fig. 7d), but strong northerly anomalies during the preconditioning phase (Fig. 7g), indicating a different  
376 temporal phasing between circulation anomalies and peak warming. These patterns suggest that while  
377 elevated mid-tropospheric geopotential heights are a common precursor to extreme warm events,  
378 differences in the strength, location, and timing of low-level meridional flow likely modulate the magnitude  
379 and spatial footprint of surface warming through thermal advection and interactions with AP topography  
380 that favour föhn-like warming in some regions.

### 381 **3.4 Role of thermal advection for high temperature events**

382 Figure 8 quantifies the anomalous upper tropospheric horizontal thermal advection associated with  
383 extreme high AP temperature events for each cluster. In the days immediately preceding event onset, all  
384 clusters exhibit pronounced positive horizontal thermal advection to the west of the AP, locally exceeding  
385  $4 \text{ K day}^{-1}$  (Fig. 8f-j). These strong warming tendencies represent a marked intensification from the  
386 preconditioning period, during which comparable advection magnitudes occur only in Cluster 3, across  
387 the Bellingshausen Sea and centred near  $\sim 50^\circ\text{S}$  west of South America (Fig. 8c). Although all clusters  
388 show anomalous warming tendencies in the region of the AP, as anticipated, their spatial structures differ.  
389 Cluster 5 displays weaker and more geographically confined warming, with anomalies of  $\sim 3 \text{ K day}^{-1}$   
390 largely restricted to the AP region. In contrast, Clusters 1-4 exhibit broader horizontal advection patterns  
391 extending from further west across the Bellingshausen Sea. Across all clusters, anomalous negative  
392 meridional advection (cooling) occurs over the Weddell Sea, consistent with anomalous southerly flow in  
393 that region.

394



395

396 **Figure 8: As in Figure 6, but for anomalies in 300 hPa horizontal thermal advection (shading) and**  
 397 **wind speed (vectors) for the sector 105°W - 45°W , 45°S - 80°S.**

398 Following event onset (Fig. 8k–o), more pronounced cluster-dependent behaviour emerges. Cluster 2  
 399 shows widespread positive advection across much of the AP, whereas Clusters 1 and 4 continue to be  
 400 dominated by warming originating from the lower-latitude Bellingshausen Sea. In Cluster 3, the advection  
 401 signal weakens across the Bellingshausen Sea region substantially after onset whilst showing warming in  
 402 the Weddell Sea and north of AP; this is also seen in Cluster 5.

403 A decomposition of the anomalous upper tropospheric thermal advection for all high temperature events  
 404 reveals that the meridional component is dominant and this is largely explained by anomalous meridional  
 405 wind anomalies (Fig. S6). In the zonal component, zonal wind anomalies contribute more than variations  
 406 in the zonal temperature gradient. These results indicate that anomalous warming during extreme events  
 407 is driven primarily by changes in flow strength and direction, rather than by modulation of the background  
 408 temperature gradients.

409 Together, these results provide further evidence that enhanced poleward heat transport via anomalous  
 410 meridional flow is a fundamental mechanism underpinning extreme warm events across all clusters, while  
 411 differences in the location, magnitude, and persistence of this advection help put into context the  
 412 contrasting growth rates, spatial footprints, and lifetimes of temperature anomalies.

413 **4 Discussion**

414



415 González et al. (2018) identified five recurrent synoptic-scale circulation patterns over the Drake Passage  
416 and AP region using a similar method applied over the full annual cycle. These included patterns  
417 characterised by low pressure in the Weddell Sea, Amundsen–Bellingshausen Seas, and Drake  
418 Passage, as well as zonal flow and a ridge over the AP. Our results suggest that extreme high AP  
419 temperatures in austral summer are associated with a subset of the broad circulation regimes identified  
420 by González et al. (2018), particularly those featuring ridging over or immediately upstream of the AP. To  
421 draw further comparison, they find that a cluster featuring a low over the Drake Passage is the most  
422 frequent pattern during austral summer, followed by a more zonally oriented flow, which qualitatively  
423 agrees with our findings where Cluster 5 is the most abundant cluster, albeit with its low centre of action  
424 located further north. Furthermore, we identify circulation patterns specifically associated with extreme  
425 high AP temperature events that were not separated in González et al. (2018); for example conditioning  
426 on temperature extremes can reveal additional nuances in the patterns of synoptic scale flow during  
427 extreme events such as between clusters 2 and 4, which might otherwise be grouped into a single broad  
428 cluster. In this sense, the present study extends González et al. (2018) by demonstrating how specific  
429 synoptic patterns are selectively associated with temperature extremes, and by documenting the distinct  
430 dynamical signatures associated with each extreme-favouring regime.

431

432 The hemispheric-scale atmospheric circulation anomalies show signatures consistent with zonal  
433 wavenumber-3 and wavenumber-2 patterns, demonstrated in cluster 1 and clusters 2 and 4, respectively,  
434 indicating a hemispheric-scale connection through planetary-scale Rossby wave trains between the  
435 tropics, midlatitudes and polar regions (e.g., Ding and Steig 2013; Boschat et al., 2023; Goyal et al.,  
436 2021). Such wave trains are frequently initiated by anomalous tropical convection associated with ENSO  
437 and the MJO (e.g. Lee and Seo, 2019; Schneider et al., 2012), and can promote persistent blocking highs  
438 over the South Pacific and Drake Passage that favour warm air advection toward the AP (Rondanelli et  
439 al., 2019; Clem et al., 2022). Nevertheless, there is evidence to suggest that there is a spatial  
440 dependency regarding the impacts of the different modes of climate variability on regions of the AP (e.g.  
441 Clem and Fogt., 2013; Clem et al., 2016). Our results suggest a role for planetary scale modes in driving  
442 high AP temperature events. In particular, Cluster 4 exhibits a more persistent and extensive high-  
443 pressure anomaly over Antarctica in the lead-up to the onset of extreme warm temperatures across AP,  
444 suggestive of a negative SAM-like state, which is known to weaken the circumpolar westerlies and shift  
445 the storm track equatorward, thereby promoting warm air intrusions into the AP (Turner et al., 2013;  
446 Raphael et al., 2016). This is consistent with well established evidence that variations in SAM strongly  
447 modulate AP temperature extremes (Fogt et al., 2012; Clem et al., 2016; Turner et al., 2020).

448

449 The spatial footprint of warming differs markedly between clusters, with some exhibiting continent-wide  
450 warming while others show warming largely confined to West Antarctica or the AP alone. This behaviour  
451 mirrors continental-scale analyses showing that West Antarctic temperature extremes tend to be spatially



452 confined and closely linked to meridional flow anomalies, whereas East Antarctic temperature extremes  
453 are often associated with inland high-pressure systems and katabatic wind enhancement (Nielsen et al.,  
454 2025). The present results support this evidence and suggest that the AP occupies a dynamical regime in  
455 which both large-scale advection and local topographic effects strongly influence extreme temperature  
456 expression.

457

458 Our results have shown that large-scale thermal advection plays a key role in driving high temperature  
459 events on the AP. Station-based analyses indicate that the majority of record local temperature extremes  
460 on the AP occur following flow across steep orography, consistent with an important contribution from  
461 föhn warming (Turner et al., 2020). In addition, the presence of high pressure and near-surface wind  
462 anomalies extending for several days over the AP, particularly in Clusters 1 and 5, supports a mechanism  
463 whereby anomalous anticyclonic flow drives warm, dry northwesterly winds onto the upwind side of the  
464 AP, producing föhn-like conditions on the leeward side. ERA5 does not fully resolve the dynamics of föhn  
465 flow due to its coarse spatial resolution, however, the presence of northwesterly low-level wind anomalies  
466 in several clusters suggests there would be a central role of föhn processes in the high AP temperature  
467 events identified as found in various studies (Elvidge et al., 2014; Laffin et al. 2021; Turton et al., 2018).  
468 These dynamics are well-established contributors to surface melt and firn air depletion on the AP (e.g.  
469 Cape et al., 2015; Zou et al., 2023; Kirchgassner et al., 2021), and have been implicated in major melt  
470 events over ice shelves such as Larsen C (Elvidge et al., 2014). Case study events pertaining to each  
471 cluster, using observations and high-resolution modelling tools such as dynamically downscaled regional  
472 climate model outputs, should be looked at in future to help understand the relative role of local-scale  
473 (föhn wind) from background forcing due to large-scale drivers.

474

## 475 **5 Conclusions**

476

477 This study has identified five distinct circulation patterns associated with extreme high summer  
478 temperatures across AP in austral summer using k-means clustering applied to daily MSLP on days when  
479 the 2-m AP averaged temperature exceeds the 95th percentile. The resulting clusters exhibit substantial  
480 diversity in the patterns of continental 2-m temperature, 10-m wind, and mid-tropospheric geopotential  
481 height anomalies, demonstrating that high temperature extremes on the AP are driven by a range of  
482 synoptic circulation states. While Cluster 4 shows continent-wide warming, Clusters 1 and 3 show  
483 warming confined to WA. The warming in Cluster 2 and 5 is more confined to the AP with coincident  
484 cooling across parts of EA. Unsurprisingly, all clusters are associated with a ridge over the northern AP,  
485 though the magnitude, orientation and persistence of this feature varies significantly.

486

487 The classification of dynamical patterns associated with similar high AP summer temperatures extends  
488 prior work on circulation patterns throughout the seasonal cycle (Gonzalez et al., 2018) and continental



489 trends and extremes (Turner et al., 2020; Nielsen et al., 2025) and reveals that extreme high AP  
490 temperatures arise not from a single canonical pattern, but from a range of distinct synoptic states. Future  
491 work could examine the connection of these states to remote large-scale drivers such as tropical and  
492 subtropical convection (e.g., Turner et al., 2016; Pezza et al. 2012), the SAM and the stratospheric polar  
493 vortex (e.g., Lim et al., 2018), as well as assess their representation in climate models in order to better  
494 understand their predictability across future timescales.

495

496 While this study has applied k-means clustering to circulation fields in order to focus on the role of  
497 atmospheric dynamics, it may be interesting in the future to include other information in the clustering  
498 related to thermodynamic preconditioning and radiative effects, which have been shown to contribute to  
499 extreme melt and temperature events (e.g. Gorodetskaya et al., 2023; Wille et al., 2022), and to quantify  
500 thermal tendencies from adiabatic descent, turbulent mixing, and cloud-radiative effects.

501

#### 502 **Data Availability Statement**

503

504 The ERA5 reanalysis data sets (Hersbach et al., 2020) can be obtained from the Copernicus Climate  
505 Data Store (<https://cds.climate.copernicus.eu/>). All figures are prepared using Python (version 3.11).

506

#### 507 **Author Contributions**

508

509 WJD, ACM and ANR designed the study. WJD performed the analysis and produced the figures. WJD  
510 wrote the manuscript draft; ACM and ANR edited the manuscript with comments from RSW, TJB.

511

#### 512 **Competing Interests**

513

514 The contact author has declared that none of the authors have any competing interests.

#### 515 **Acknowledgements**

516

517 We are grateful to the wider NERC-funded ExtAnt project team for their contributions to the discussion of  
518 the results. We thank Tony Phillips for assistance with data handling. We are also grateful to NERC's  
519 JASMIN facility for providing resources to conduct the analysis.

520

#### 521 **Financial Support**

522

523 All authors were funded as part of the ExtAnt project (NERC grants NE/Y503307/1 and NE/Y503319/1).

524



525 **References**

526

527 Baba, K., & Renwick, J. (2017). Aspects of intraseasonal variability of Antarctic sea ice in austral winter  
528 related to ENSO and SAM events. *Journal of Glaciology*, 63(241), 838–846.

529 <https://doi.org/10.1017/JOG.2017.49>

530

531 Bae, H. J., Kim, S. J., Kim, B. M., & Kwon, H. (2022). Causes of the Extreme Hot Event on February 9,  
532 2020, in Seymour Island, Antarctic Peninsula. *Frontiers in Environmental Science*, 10, 865775.

533 <https://doi.org/10.3389/FENVS.2022.865775>

534

535 Balay, F., & Renom, M. (2026). Characterization of extreme warm temperature events (1998–2016) on  
536 King George Island, Antarctic Peninsula. *Antarctic Science*, 00, 1–15.

537 <https://doi.org/10.1017/S0954102025100552>

538

539 Baldwin, J. W., Dessy, J. B., Vecchi, G. A., & Oppenheimer, M. (2019). Temporally Compound Heat  
540 Wave Events and Global Warming: An Emerging Hazard. *Earth's Future*, 7(4), 411–427.

541 <https://doi.org/10.1029/2018EF000989>

542

543 Banwell, A. F., Tri Datta, R., Dell, R. L., Moussavi, M., Brucker, L., Picard, G., Shuman, C. A., & Stevens,  
544 L. A. (2021). The 32-year record-high surface melt in 2019/2020 on the northern George VI Ice Shelf,  
545 Antarctic Peninsula. *Cryosphere*, 15(2), 909–925. <https://doi.org/10.5194/TC-15-909-2021>,

546

547 Barrett, B. S., Lafleur, D. M., & Henderson, G. R. (2025). Madden–Julian Oscillation Modulation of  
548 Antarctic Sea Ice. *Glaciers 2025*, Vol. 2, 2(4), 16. <https://doi.org/10.3390/GLACIES2040016>

549

550 Bevan, S., Luckman, A., Hendon, H., & Wang, G. (2020). The 2020 Larsen C Ice Shelf surface melt is a  
551 40-year record high. *Cryosphere*, 14(10), 3551–3564. <https://doi.org/10.5194/TC-14-3551-2020>,

552

553 Boschat, G., Purich, A., Rudeva, I., & Arblaster, J. (2023). Impact of Zonal and Meridional Atmospheric  
554 Flow on Surface Climate and Extremes in the Southern Hemisphere. *Journal of Climate*, 36(15), 5041–  
555 5061. <https://doi.org/10.1175/JCLI-D-22-0251.1>

556

557 Bozkurt, D., Bromwich, D. H., Carrasco, J., Hines, K. M., Maureira, J. C., & Rondanelli, R. (2020). Recent  
558 Near-surface Temperature Trends in the Antarctic Peninsula from Observed, Reanalysis and Regional  
559 Climate Model Data. *Advances in Atmospheric Sciences*, 37(5), 477–493.

560 <https://doi.org/10.1007/S00376-020-9183-X/>

561



- 562 Bozkurt, D., Marin, J. C., Verdugo, C., & Barrett, B. S. (2024). Atmospheric blocking and temperatures in  
563 the Antarctic Peninsula. *Science of The Total Environment*, 931, 172852.  
564 <https://doi.org/10.1016/J.SCITOTENV.2024.172852>  
565
- 566 Bracegirdle, T. J., Caton Harrison, T., Holmes, C. R., Lu, H., Martineau, P., & Phillips, T. (2024). Antarctic  
567 extreme seasons under 20th and 21st century climate change. *Npj Climate and Atmospheric Science*,  
568 7(1), 1–12.  
569 <https://doi.org/10.1038/S41612-024-00822-Y>  
570
- 571 Cape, M. R., Vernet, M., Skvarca, P., Marinsek, S., Scambos, T., & Domack, E. (2015). Foehn winds link  
572 climate-driven warming to ice shelf evolution in Antarctica. *Journal of Geophysical Research:*  
573 *Atmospheres*, 120(21), 11,037–11,057. <https://doi.org/10.1002/2015JD023465>  
574
- 575 Carrasco, J. F., Bozkurt, D., & Cordero, R. R. (2021). A review of the observed air temperature in the  
576 Antarctic Peninsula. Did the warming trend come back after the early 21st hiatus? *Polar Science*, 28,  
577 100653. <https://doi.org/10.1016/j.polar.2021.100653>  
578
- 579 Clem, K. R., Renwick, J. A., McGregor, J., & Fogt, R. L. (2016). The relative influence of ENSO and SAM  
580 on Antarctic Peninsula climate. *Journal of Geophysical Research: Atmospheres*, 121(16), 9324–  
581 9341. <https://doi.org/10.1002/2016JD025305>  
582
- 583 Clem, K.R., Bozkurt, D., Kennett, D. et al. Central tropical Pacific convection drives extreme high  
584 temperatures and surface melt on the Larsen C Ice Shelf, Antarctic Peninsula. *Nat. Commun* 13, 3906  
585 (2022). <https://doi.org/10.1038/s41467-022-31119-4>  
586
- 587 Clem, K. R., & Fogt, R. L. (2013). Varying roles of ENSO and SAM on the Antarctic Peninsula climate in  
588 austral spring. *Journal of Geophysical Research Atmospheres*, 118(20), 11,481–11,492.  
589 <https://doi.org/10.1002/JGRD.50860>  
590
- 591 Clem, K. R., Renwick, J. A., McGregor, J., & Fogt, R. L. (2016). The relative influence of ENSO and SAM  
592 on Antarctic Peninsula climate. *Journal of Geophysical Research*, 121(16), 9324–9341.  
593 <https://doi.org/10.1002/2016JD025305:PAGE:STRING:ARTICLE/CHAPTER>  
594
- 595 Coggins, J. H. J., McDonald, A. J., & Jolly, B. (2014). Synoptic climatology of the Ross Ice Shelf and Ross  
596 Sea region of Antarctica: K-means clustering and validation. *International Journal of Climatology*, 34(7),  
597 2330–2348. <https://doi.org/10.1002/JOC.3842>  
598



- 599 DeConto, R. M., & Pollard, D. (2016). Contribution of Antarctica to past and future sea-level rise. *Nature*,  
600 531(7596), 591–597. <https://doi.org/10.1038/NATURE17145>  
601
- 602 Deb, P., Bromwich, D., Orr, A., Sen, A., & Clem, K. R. (2025). Recent increase in surface melting of West  
603 Antarctic ice shelves linked to Interdecadal Pacific Oscillation. *Communications Earth & Environment*  
604 2025 6:1, 6(1), 99-. <https://doi.org/10.1038/s43247-025-02077-8>  
605
- 606 Ding, Q., & Steig, E. J. (2013). Temperature Change on the Antarctic Peninsula Linked to the Tropical  
607 Pacific. *Journal of Climate*, 26(19), 7570–7585. <https://doi.org/10.1175/JCLI-D-12-00729.1>  
608
- 609 Ding, Q., Steig, E., Battisti, D., & Küttel, M. (2011). Winter warming in West Antarctica caused by central  
610 tropical Pacific warming. *Nature Geoscience*. <https://doi.org/10.1038/NGEO1129>  
611
- 612 Dunmire, D., Wever, N., Banwell, A. F., & Lenaerts, J. T. M. (2024). Antarctic-wide ice-shelf firn emulation  
613 reveals robust future firn air depletion signal for the Antarctic Peninsula. *Communications Earth and*  
614 *Environment*, 5(1), 1–13. <https://doi.org/10.1038/S43247-024-01255-4>  
615
- 616 Elvidge, A. D., Renfrew, I. A., King, J. C., Orr, A., Lachlan-Cope, T. A., Weeks, M., & Gray, S. L. (2014).  
617 Foehn jets over the Larsen C Ice Shelf, Antarctica. *Quarterly Journal of the Royal Meteorological Society*,  
618 141(688), 698–713. <https://doi.org/10.1002/QJ.2382>  
619
- 620 England, M. R., Polvani, L. M., Smith, K. L., Landrum, L., & Holland, M. M. (2016). Robust response of  
621 the Amundsen Sea Low to stratospheric ozone depletion. *Geophysical Research Letters*, 43(15), 8207–  
622 8213. <https://doi.org/10.1002/2016GL070055>  
623
- 624 Feron, S., Cordero, R. R., Damiani, A., Malhotra, A., Seckmeyer, G., & Llanillo, P. (2021). Warming  
625 events projected to become more frequent and last longer across Antarctica. *Scientific Reports*, 11(1), 1–  
626 9. <https://doi.org/10.1038/S41598-021-98619-Z>  
627
- 628 Fogt, R. L., Bromwich, D. H., & Hines, K. M. (2010). Understanding the SAM influence on the South  
629 Pacific ENSO teleconnection. *Climate Dynamics* 2010 36:7, 36(7), 1555–1576.  
630 <https://doi.org/10.1007/S00382-010-0905-0>  
631
- 632 Fogt, R. L., Jones, J. M., & Renwick, J. (2012). Seasonal Zonal Asymmetries in the Southern Annular  
633 Mode and Their Impact on Regional Temperature Anomalies. *Journal of Climate*, 25(18), 6253–6270.  
634 <https://doi.org/10.1175/JCLI-D-11-00474.1>  
635



- 636 Fogt, R. L., & Marshall, G. J. (2020). The Southern Annular Mode: Variability, trends, and climate impacts  
637 across the Southern Hemisphere. *Wiley Interdisciplinary Reviews: Climate Change*, 11(4), e652.  
638 <https://doi.org/10.1002/WCC.652>:ISSUE:ISSUE:DOI  
639
- 640 Hosking, J. S., Orr, A., Marshall, G. J., Turner, J., & Phillips, T. (2013). The Influence of the Amundsen–  
641 Bellingshausen Seas Low on the Climate of West Antarctica and Its Representation in Coupled Climate  
642 Model Simulations. *Journal of Climate*, 26(17), 6633–6648. <https://doi.org/10.1175/JCLI-D-12-00813.1>  
643
- 644 Gonzalez, S., & Fortuny, D. (2018). How robust are the temperature trends on the Antarctic Peninsula?  
645 *Antarctic Science*, 30(5), 322–328. <https://doi.org/10.1017/S0954102018000251>  
646
- 647 Gonzalez, S., Vasallo, F., Recio-Blitz, C., Guijarro, J. A., & Riesco, J. (2018). Atmospheric Patterns over  
648 the Antarctic Peninsula. *Journal of Climate*, 31(9), 3597–3608. <https://doi.org/10.1175/JCLI-D-17-0598.1>  
649
- 650 González-Herrero, S., Barriopedro, D., Trigo, R. M., López-Bustins, J. A., & Oliva, M. (2022). Climate  
651 warming amplified the 2020 record-breaking heatwave in the Antarctic Peninsula. *Communications Earth  
652 & Environment* 2022 3:1, 3(1), 122-. <https://doi.org/10.1038/s43247-022-00450-5>  
653
- 654 González-Herrero, S., Vasallo, F., Bech, J., Gorodetskaya, I., Elvira, B., & Justel, A. (2023). Extreme  
655 precipitation records in Antarctica. *International Journal of Climatology*, 43(7), 3125–3138.  
656 <https://doi.org/10.1002/JOC.8020>  
657
- 658 Gorodetskaya, I. v, Durán-Alarcón, C., González-Herrero, S., Clem, K. R., Zou, X., Rowe, P., Rodriguez  
659 Imazio, P., Campos, D., Leroy, C., Santos, -Dos, Dutrievoz, N., Wille, J. D., Chyhareva, A., Favier, V.,  
660 Blanchet, J., Pohl, B., Cordero, R. R., Park, S.-J., Colwell, S., ... Picard, G. (2023). Record-high Antarctic  
661 Peninsula temperatures and surface melt in February 2022: a compound event with an intense  
662 atmospheric river. *Npj Climate and Atmospheric Science* 2023 6:1, 6(1), 1–18.  
663 <https://doi.org/10.1038/s41612-023-00529-6>  
664
- 665 Goyal, R., Jucker, M., sen Gupta, A., Hendon, H. H., & England, M. H. (2021). Zonal wave 3 pattern in the  
666 Southern Hemisphere generated by tropical convection. *Nature Geoscience* 2021 14:10, 14(10), 732–  
667 738. <https://doi.org/10.1038/s41561-021-00811-3>  
668
- 669 Guarino, M.-V., Ridley, J. K., Colwell, S., Farneti, R., Giuliani, G., Hindley, N., King, J., Kucharski, F.,  
670 Polichtchouk, I., Tompkins, A. M., Vignon, É., Wright, C., Guarino, M.-V., Ridley, J. K., Colwell, S.,  
671 Farneti, R., Giuliani, G., Hindley, N., King, J., ... Wright, C. (2026). A Long-Term Shift in Flow Regimes  
672 over the Antarctic Peninsula. *Journal of Climate*, 39(2), 749–767. <https://doi.org/10.1175/jcli-d-25-0330.1>



- 673
- 674 Hillebrand, F. L., Bremer, U. F., Arigony-Neto, J., da Rosa, C. N., Mendes, C. W., Costi, J., de Freitas, M.  
675 W. D., & Schardong, F. (2021). Comparison between Atmospheric Reanalysis Models ERA5 and ERA-  
676 Interim at the North Antarctic Peninsula Region. *Annals of the American Association of Geographers*,  
677 111(4), 1147–1159. <https://doi.org/10.1080/24694452.2020.1807308>  
678
- 679 Hersbach, H., Bell, B., Berrisford, P., Hirahara, S., Horányi, A., Muñoz-Sabater, J., Nicolas, J., Peubey,  
680 C., Radu, R., Schepers, D., Simmons, A., Soci, C., Abdalla, S., Abellan, X., Balsamo, G., Bechtold, P.,  
681 Biavati, G., Bidlot, J., Bonavita, M., ... Thépaut, J. N. (2020). The ERA5 global reanalysis. *Quarterly*  
682 *Journal of the Royal Meteorological Society*, 146(730), 1999–2049. <https://doi.org/10.1002/qj.3803>  
683
- 684 Jones, M. E., Bromwich, D. H., Nicolas, J. P., Carrasco, J., Plavcová, E., Zou, X., & Wang, S. H. (2019).  
685 Sixty Years of Widespread Warming in the Southern Middle and High Latitudes (1957–2016). *Journal of*  
686 *Climate*, 32(20), 6875–6898. <https://doi.org/10.1175/JCLI-D-18-0565.1>  
687
- 688 Kirchgaessner, A., King, J. C., & Anderson, P. S. (2021). The Impact of Föhn Conditions Across the  
689 Antarctic Peninsula on Local Meteorology Based on AWS Measurements. *Journal of Geophysical*  
690 *Research: Atmospheres*, 126(4), e2020JD033748. <https://doi.org/10.1029/2020JD033748>  
691
- 692 Laffin, M. K., Zender, C. S., Singh, S., van Wessem, J. M., Smeets, C. J. P. P., & Reijmer, C. H. (2021).  
693 Climatology and Evolution of the Antarctic Peninsula Föhn Wind-Induced Melt Regime From 1979–2018.  
694 *Journal of Geophysical Research: Atmospheres*, 126(4), e2020JD033682.  
695 <https://doi.org/10.1029/2020JD033682>  
696
- 697 Lee, H. J., & Seo, K. H. (2019). Impact of the Madden-Julian oscillation on Antarctic sea ice and its  
698 dynamical mechanism. *Scientific Reports 2019 9:1*, 9(1), 10761-. [https://doi.org/10.1038/s41598-019-](https://doi.org/10.1038/s41598-019-47150-3)  
699 [47150-3](https://doi.org/10.1038/s41598-019-47150-3)  
700
- 701 Li, X., Gerber, E. P., Holland, D. M., & Yoo, C. (2015). A Rossby Wave Bridge from the Tropical Atlantic  
702 to West Antarctica. *Journal of Climate*, 28(6), 2256–2273. <https://doi.org/10.1175/JCLI-D-14-00450.1>  
703
- 704 Li, X., Holland, D. M., Gerber, E. P., & Yoo, C. (2014). Impacts of the north and tropical Atlantic Ocean on  
705 the Antarctic Peninsula and sea ice. *Nature*, 505(7484), 538–542.  
706 <https://doi.org/10.1038/NATURE12945;TECHMETA>  
707
- 708 Lim, E. P., Hendon, H. H., & Thompson, D. W. J. (2018). Seasonal Evolution of Stratosphere-  
709 Troposphere Coupling in the Southern Hemisphere and Implications for the Predictability of Surface



- 710 Climate. *Journal of Geophysical Research: Atmospheres*, 123(21), 12,002–12,016.  
711 <https://doi.org/10.1029/2018JD029321>  
712  
713 Marshall, G. J. (2003). Trends in the southern annular mode from observations and reanalyses. *Journal*  
714 *of Climate*, 16(24), 4134–4143. [https://doi.org/10.1175/1520-0442\(2003\)016<4134:TITSAM>2.0.CO;2](https://doi.org/10.1175/1520-0442(2003)016<4134:TITSAM>2.0.CO;2)  
715  
716 Marshall, G. J. (2007). Half-century seasonal relationships between the Southern Annular Mode and  
717 Antarctic temperatures. *International Journal of Climatology*, 27(3), 373–383.  
718 <https://doi.org/10.1002/JOC.1407>  
719  
720 Marshall, G. J., Fogt, R. L., Turner, J., & Clem, K. R. (2022). Can current reanalyses accurately portray  
721 changes in Southern Annular Mode structure prior to 1979? *Climate Dynamics* 2022 59:11, 59(11), 3717–  
722 3740. <https://doi.org/10.1007/s00382-022-06292-3>  
723  
724 Marshall, G. J., Orr, A., van Lipzig, N. P. M., & King, J. C. (2006). The Impact of a Changing Southern  
725 Hemisphere Annular Mode on Antarctic Peninsula Summer Temperatures. *Journal of Climate*, 19(20),  
726 5388–5404. <https://doi.org/10.1175/JCLI3844.1>  
727  
728 Montañó Bello, D., Villegas Bolaños, N. L., (2025). Influence of ENSO and SAM on the occurrence of  
729 absolute extremes and behavior of Ta, SST, and SIC anomalies in the western Antarctic Peninsula.  
730 *Atmósfera*, 39, 437–450. <https://doi.org/10.20937/ATM.53423>  
731  
732 Nielsen, E. B., Katurji, M., Zawar-Reza, P., & Cullen, N. (2025). Air Temperature Trends and Extreme  
733 Warming Events Across Regions of Antarctica for the Period 2003–2021. *Journal of Geophysical*  
734 *Research: Atmospheres*, 130(9), e2024JD043042. <https://doi.org/10.1029/2024JD043042>  
735  
736 Oliva, M., Navarro, F., Hrbáček, F., Hernández, A., Nývlt, D., Pereira, P., Ruiz-Fernández, J., & Trigo, R.  
737 (2017). Recent regional climate cooling on the Antarctic Peninsula and associated impacts on the  
738 cryosphere. *Science of The Total Environment*, 580, 210–223.  
739 <https://doi.org/10.1016/J.SCITOTENV.2016.12.030>  
740  
741 Orr, A., Marshall, G. J., Hunt, J. C. R., Sommeria, J., Wang, C. G., van Lipzig, N. P. M., Cresswell, D., &  
742 King, J. C. (2008). Characteristics of Summer Airflow over the Antarctic Peninsula in Response to Recent  
743 Strengthening of Westerly Circumpolar Winds. *Journal of the Atmospheric Sciences*, 65(4), 1396–1413.  
744 <https://doi.org/10.1175/2007JAS2498.1>  
745



- 746 Pezza, A. B., Rashid, H. A., & Simmonds, I. (2012). Climate links and recent extremes in antarctic sea  
747 ice, high-latitude cyclones, Southern Annular Mode and ENSO. *Climate Dynamics*, 38(1–2), 57–73.  
748 <https://doi.org/10.1007/S00382-011-1044-Y/>  
749
- 750 Raphael, M. N., Marshall, G. J., Turner, J., Fogt, R. L., Schneider, D., Dixon, D. A., Hosking, J. S., Jones,  
751 J. M., & Hobbs, W. R. (2016). The Amundsen Sea Low: Variability, Change, and Impact on Antarctic  
752 Climate. *Bulletin of the American Meteorological Society*, 97(1), 111–121. [https://doi.org/10.1175/BAMS-](https://doi.org/10.1175/BAMS-D-14-00018.1)  
753 [D-14-00018.1](https://doi.org/10.1175/BAMS-D-14-00018.1)  
754
- 755 Renwick JA, Revell MJ (1999) Blocking over the South Pacific and Rossby wave propagation. *Mon*  
756 *Weather Rev* 127(10):2233–2247. [https://doi.org/10.1175/1520-0493\(1999\)127<2233:BOTSPA>2.0.CO;2](https://doi.org/10.1175/1520-0493(1999)127<2233:BOTSPA>2.0.CO;2)  
757
- 758 Rondanelli, R., Hatchett, B., Rutllant, J., Bozkurt, D., & Garreaud, R. (2019). Strongest MJO on record  
759 triggers extreme Atacama rainfall and warmth in Antarctica. *Geophysical Research Letters*, 46, 3482-  
760 3491. <https://doi.org/10.1029/2018GL081475>  
761
- 762 Rousseeuw, P. J. (1987). Silhouettes: A graphical aid to the interpretation and validation of cluster  
763 analysis. *Journal of Computational and Applied Mathematics*, 20(C), 53–65. [https://doi.org/10.1016/0377-](https://doi.org/10.1016/0377-0427(87)90125-7)  
764 [0427\(87\)90125-7](https://doi.org/10.1016/0377-0427(87)90125-7)  
765
- 766 Ruosteenoja, K., & Jylhä, K. (2023). Average and extreme heatwaves in Europe at 0.5–2.0 °C global  
767 warming levels in CMIP6 model simulations. *Climate Dynamics*, 61(9–10), 4259–4281.  
768 <https://doi.org/10.1007/S00382-023-06798-4/>  
769
- 770 Sadai, S., Condron, A., DeConto, R., & Pollard, D. (2020). Future climate response to Antarctic Ice Sheet  
771 melt caused by anthropogenic warming. *Science Advances*, 6(39).  
772 [https://doi.org/10.1126/SCIADV.AAZ1169/SUPPL\\_FILE/AAZ1169\\_SM.PDF](https://doi.org/10.1126/SCIADV.AAZ1169/SUPPL_FILE/AAZ1169_SM.PDF)  
773
- 774 Scambos, T., Fricker, H. A., Liu, C. C., Bohlander, J., Fastook, J., Sargent, A., Massom, R., & Wu, A. M.  
775 (2009). Ice shelf disintegration by plate bending and hydro-fracture: Satellite observations and model  
776 results of the 2008 Wilkins ice shelf break-ups. *Earth and Planetary Science Letters*, 280(1–4), 51–60.  
777 <https://doi.org/10.1016/J.EPSL.2008.12.027>  
778
- 779 Schneider, D. P., Deser, C., & Okumura, Y. (2012). An assessment and interpretation of the observed  
780 warming of West Antarctica in the austral spring. *SpringerDP Schneider, C Deser, Y OkumuraClimate*  
781 *Dynamics, 2012•Springer*, 38(1–2), 323–347. <https://doi.org/10.1007/S00382-010-0985-X>  
782



- 783 Siegert, M., Atkinson, A., Banwell, A., Brandon, M., Convey, P., Davies, B., Downie, R., Edwards, T.,  
784 Hubbard, B., Marshall, G., Rogelj, J., Rumble, J., Stroeve, J., & Vaughan, D. (2019). The Antarctic  
785 Peninsula under a 1.5°C global warming scenario. *Frontiers in Environmental Science*, 7(JUN), 465700.  
786 <https://doi.org/10.3389/FENV.S.2019.00102>  
787
- 788 Tetzner, D., Thomas, E., & Allen, C. (2019). A Validation of ERA5 Reanalysis Data in the Southern  
789 Antarctic Peninsula—Ellsworth Land Region, and Its Implications for Ice Core Studies. *Geosciences*  
790 2019, Vol. 9, Page 289, 9(7), 289. <https://doi.org/10.3390/GEOSCIENCES9070289>  
791
- 792 Tewari, K., Mishra, S. K., Salunke, P., & Dewan, A. (2022). Future projections of temperature and  
793 precipitation for Antarctica. *Environmental Research Letters*, 17(1), 014029. <https://doi.org/10.1088/1748-9326/AC43E2>  
794  
795
- 796 Thompson, D. W. J., & Solomon, S. (2002). Interpretation of recent Southern Hemisphere climate  
797 change. *Science.orgDWJ Thompson, S SolomonScience, 2002•science.Org, 296(5569)*, 895–899.  
798 <https://doi.org/10.1126/SCIENCE.1069270>  
799
- 800 Tseng, K. C., Maloney, E., & Barnes, E. (2019). The Consistency of MJO Teleconnection Patterns: An  
801 Explanation Using Linear Rossby Wave Theory. *Journal of Climate*, 32(2), 531–548.  
802 <https://doi.org/10.1175/JCLI-D-18-0211.1>  
803
- 804 Turner, J., Barrand, N. E., Bracegirdle, T. J., Convey, P., Hodgson, D. A., Jarvis, M., Jenkins, A.,  
805 Marshall, G., Meredith, M. P., Roscoe, H., Shanklin, J., French, J., Goosse, H., Guglielmin, M., Gutt, J.,  
806 Jacobs, S., Kennicutt, M. C., Masson-Delmotte, V., Mayewski, P., ... Klepikov, A. (2014). Antarctic  
807 climate change and the environment: an update. *Polar Record*, 50(3), 237–259.  
808 <https://doi.org/10.1017/S0032247413000296>  
809
- 810 Turner, J., Colwell, S. R., Marshall, G. J., Lachlan-Cope, T. A., Carleton, A. M., Jones, P. D., Lagun, V.,  
811 Reid, P. A., & lagovkina, S. (2005). Antarctic climate change during the last 50 years. *International*  
812 *Journal of Climatology*, 25(3), 279–294. <https://doi.org/10.1002/JOC.1130>  
813
- 814 Turner, J., Lu, H., White, I., King, J. C., Phillips, T., Hosking, J. S., Bracegirdle, T. J., Marshall, G. J.,  
815 Mulvaney, R., & Deb, P. (2016). Absence of 21st century warming on Antarctic Peninsula consistent with  
816 natural variability. *Nature*, 535(7612), 411–415. <https://doi.org/10.1038/NATURE18645>  
817



- 818 Turner, J., Maksym, T., Phillips, T., Marshall, G. J., & Meredith, M. P. (2013). The impact of changes in  
819 sea ice advance on the large winter warming on the western Antarctic Peninsula. *International Journal of*  
820 *Climatology*, 33(4), 852–861. <https://doi.org/10.1002/JOC.3474>  
821
- 822 Turner, J., Marshall, G. J., Clem, K., Colwell, S., Phillips, T., & Lu, H. (2020). Antarctic temperature  
823 variability and change from station data. *International Journal of Climatology*, 40(6), 2986–3007.  
824 <https://doi.org/10.1002/joc.6378>  
825
- 826 Turton, J. V., Kirchgaessner, A., Ross, A. N., King, J. C., & Munneke, P. K. (2020). The influence of föhn  
827 winds on annual and seasonal surface melt on the Larsen C Ice Shelf, Antarctica. *Cryosphere*, 14(11),  
828 4165–4180. <https://doi.org/10.5194/TC-14-4165-2020>  
829
- 830 Wang, J., Luo, H., Yu, L., Li, X., Holland, P. R., & Yang, Q. (2023). The Impacts of Combined SAM and  
831 ENSO on Seasonal Antarctic Sea Ice Changes. *Journal of Climate*, 36(11), 3553–3569.  
832 <https://doi.org/10.1175/JCLI-D-22-0679.1>  
833
- 834 Wang, S., Ding, M., Liu, G., Wei, T., Zhang, W., Chen, W., Dou, T., & Xiao, C. (2022a). On the drivers of  
835 temperature extremes on the Antarctic Peninsula during austral summer. *Climate Dynamics*, 59(7–8),  
836 2275–2291. <https://doi.org/10.1007/S00382-022-06209-0/>  
837
- 838 Wang, S., Ding, M., Liu, G., & Chen, W. (2022b). Processes and Mechanisms of Persistent Extreme  
839 Rainfall Events in the Antarctic Peninsula during Austral Summer. *Journal of Climate*, 35(12), 3643–3657.  
840 <https://doi.org/10.1175/JCLI-D-21-0834.1>  
841
- 842 Wille, J. D., Favier, V., Jourdain, N. C., Kittel, C., Turton, J. V., Agosta, C., Gorodetskaya, I. v., Picard, G.,  
843 Codron, F., Santos, C. L. dos, Amory, C., Fettweis, X., Blanchet, J., Jomelli, V., & Berchet, A. (2022).  
844 Intense atmospheric rivers can weaken ice shelf stability at the Antarctic Peninsula. *Communications*  
845 *Earth and Environment*, 3(1), 1–14. <https://doi.org/10.1038/S43247-022-00422-9>  
846
- 847 Xie, A., Wang, S., Xiao, C., Kang, S., Gong, J., Ding, M., Li, C., Dou, T., Ren, J., & Qin, D. (2018). *Arctic,*  
848 *Antarctic, and Alpine Research Can Temperature Extremes in East Antarctica be Replicated from ERA*  
849 *Interim Reanalysis?* <https://doi.org/10.1657/AAAR0015-048>  
850
- 851 Xu, M., Yu, L., Liang, K., Vihma, T., Bozkurt, D., Hu, X., & Yang, Q. (2021). Dominant role of vertical air  
852 flows in the unprecedented warming on the Antarctic Peninsula in February 2020. *Communications Earth*  
853 *and Environment*, 2(1), 1–9. <https://doi.org/10.1038/S43247-021-00203>  
854



855 Zhang, L., Delworth, T. L., Yang, X., Zeng, F., Lu, F., Morioka, Y., & Bushuk, M. (2022). The relative role  
856 of the subsurface Southern Ocean in driving negative Antarctic Sea ice extent anomalies in 2016–2021.  
857 *Communications Earth & Environment* 2022 3:1, 3(1), 302-. <https://doi.org/10.1038/s43247-022-00624-1>  
858  
859 Zhu, J., Xie, A., Qin, X., Wang, Y., Xu, B., & Wang, Y. (2021). An Assessment of ERA5 Reanalysis for  
860 Antarctic Near-Surface Air Temperature. *Atmosphere* 2021, Vol. 12, Page 217, 12(2), 217.  
861 <https://doi.org/10.3390/ATMOS12020217>  
862  
863 Zou, X., Rowe, P. M., Gorodetskaya, I., Bromwich, D. H., Lazzara, M. A., Cordero, R. R., Zhang, Z.,  
864 Kawzenuk, B., Cordeira, J. M., Wille, J. D., Ralph, F. M., & Bai, L. S. (2023). Strong Warming Over the  
865 Antarctic Peninsula During Combined Atmospheric River and Foehn Events: Contribution of Shortwave  
866 Radiation and Turbulence. *Journal of Geophysical Research: Atmospheres*, 128(16), e2022JD038138.  
867 <https://doi.org/10.1029/2022JD038138>  
868  
869